ACS Catalysis

Research Article

pubs.acs.org/acscatalysis

Origin of Reduced Graphene Oxide Enhancements in Electrochemical Energy Storage

James G. Radich[†] and Prashant V. Kamat*[,†,‡]

[†]Radiation Laboratory, Department of Chemical & Biomolecular Engineering and [‡]Department of Chemistry & Biochemistry, University of Notre Dame, Notre Dame, Indiana 46556, United States

Supporting Information

ABSTRACT: Reduced graphene oxide (RGO) has become a common substrate upon which active intercalation materials are anchored for electrochemical applications such as supercapacitors and lithium ion batteries. The unique attributes of RGO, including high conductivity and porous macrostructure, are often credited for enhanced cycling and capacity performance. Here we focus on probing the electrochemical response of α-MnO_2/RGO composite used as an electrode in a lithium ion battery cell and elucidating the mechanistic aspects of the RGO on the commonly observed improvements in cycling and capacity. We find that electron storage properties of RGO enables better electrode kinetics, more rapid diffusion of Li^+ to intercalation sites, and a greater capacitance effect during discharge. Further investigation of the length of the one-dimensional nanowire morphology of the α-MnO_2 has allowed us to differentiate between the innate characteristics of the MnO_2 and those of the RGO. RGO coupled with long nanowires (>5 μm) exhibited the best performance in all tests and retained ~150 mAh/g capacity after 20 cycles at 0.4C rate.

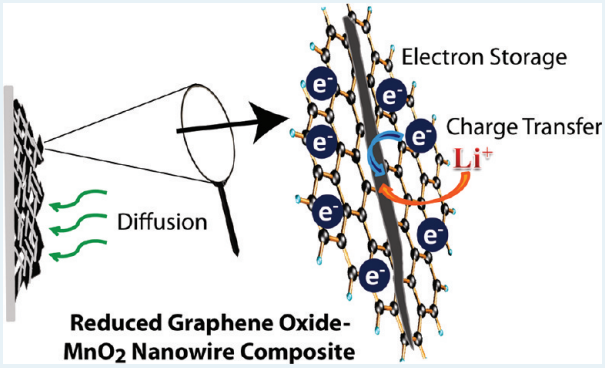

KEYWORDS: *manganese dioxide, lithium ion battery, intercalation, graphene oxide, electrode kinetics, electrochemistry*

INTRODUCTION

Rechargable lithium ion batteries are already in widespread use in applications ranging from hand-held devices to electric vehicles. Lithium ion batteries operate by shuttling Li^+ ions between intercalation host materials. Commonly, graphite is used as the negative electrode material (anode) and layered $LiCoO_2$ as the positive electrode material (cathode) in commercial secondary batteries, a design successfully pioneered and commercialized by Sony. Other cathode materials currently under investigation include the cubic spinel $LiMn_2O_4$,[1−4] the olivine $LiFePO_4$,[5−9] layered orthorhombic-$LiMnO_2$,[10−14] and even oxygen for lithium-air batteries.[15] Manganese dioxide (MnO_2), the nonlithiated version of $LiMnO_2$, is a structurally rich compound that exhibits many polymorphs, with some exhibiting various tunnel and layered structures.[16] The primary differences in the polymorphs are the coordination of MnO_6 octahedra edges and vertices, which open an array of electrochemical,[17−21] molecular sieve,[22] and catalytic applications[23−26] within the same material. MnO_2 is environmentally benign and abundant in the Earth's crust, both of which are ideal properties of high-demand materials used in batteries. Additionally, MnO_2 has the potential to yield cathode materials at significantly lower cost relative to the current standard, $LiCoO_2$, particularly if low-temperature, solution-based and scalable processes are used in the synthesis.

The α-MnO_2 polymorph exhibited good electrochemical activity in previous studies involving lithium batteries and pseudocapacitors, owing to diffusion of ions via the 2 × 2 tunnel structure. The α-MnO_2 can accommodate ions such as Li^+ and K^+ within these tunnel structures, and they provide structural stability to the octahedral arrangement.[27] Furthermore, these cations lend electronic stability to the Mn^{3+} state but also drive structural transformations due to lattice expansion depending on the stoichiometry of the cation relative to the MnO_2.[28,29] When employed in electrochemical cells, the α-MnO_2 tunnel structures enhance the reversible electrochemical response by providing pathways for rapid diffusion of Li^+ (or other ions) to active intercalation sites.[16] Prolonged polarization (used here to describe a charge-delivery bottleneck) drives instability in MnO_2 structures, as the Jahn−Teller distortion of the high-spin Mn^{3+} ion leads to disproportionation yielding Mn^{2+} and Mn^{4+}.[30] For example, low Li^+ diffusion rates coupled with rapid electron transport can render the Mn^{3+} state long-lived. This leads to disproportio-

Special Issue: Electrocatalysis

Received: February 21, 2012
Revised: March 23, 2012
Published: March 27, 2012

nation kinetics becoming dominant and thus driving electrode irreversibility.

The primary considerations toward a material's use in lithium ion batteries are cycle life retention, energy density, and discharge voltage characteristics (e.g., power delivery). Thus far the use of MnO_2 has been limited mostly to primary batteries such as the Zn-MnO_2 or Li-MnO_2 cell. Attempts to stabilize the α-MnO_2 structure for use in rechargeable batteries have focused primarily on mixed morphology synthesis,[27] doping,[31,32] and various synthesis routes yielding different morphologies or sizes.[33−35] To effectively utilize this material in secondary batteries, steps must be taken to reversibly cycle a large fraction of the 286 mAh/g theoretical energy density with good stability over many cycles.

Two major sources of electrode polarization in lithium ion batteries are concentration polarization and IR polarization. Providing effective diffusion pathways through the electrode for *both* Li^+ *and* electrons is essential to reducing these effects of polarization. Additionally, when Li^+ is the charge-delivery bottleneck, the electronic instability of the Jahn−Teller distortion is exacerbated since Li^+ intercalation provides additional electronic stability to the distorted Mn^{3+} state. Reducing these effects is important in maintaining the integrity and thus reversibility of the active material. Furthermore, good electron transport properties through the electrode to active intercalation sites will reduce IR polarization and yield higher capacity within a given voltage window.

One particular area of interest toward overcoming these problems is in using new carbon structures such as graphene as a conductive support for Li^+ insertion electrodes[36−44] along with other energy-related systems.[45] Reduced graphene oxide (RGO) is prepared via reduction of graphene oxide[46] (GO) and is similar to graphene with its partly restored sp^2 conjugated structure.[47] RGO contains defects resulting from the oxidation process and retains some residual oxygen groups, which hinders full recovery of the high conductivity associated with pristine graphene. The unique solution-processing characteristics of GO coupled with the multiple means of reduction of GO to RGO has led to a rapid increase in the use of RGO in composites for electrochemical systems. Recent publications involving the use of RGO composites for electrochemical energy storage have been reviewed.[48] Common themes arise in RGO composites for energy storage. The electrochemical performance of the intercalation material used in the study exhibits enhanced capacity as well as cycling. The two-dimensional (2-D) structure of RGO, which results in high conductivity and surface area, as well as the three-dimensional (3-D) macrostructure formed upon drying, suggests RGO is exceptionally suited for electrode applications.

Here we explore the nature of the enhancements afforded using RGO as a substrate for α-MnO_2 active material for rechargeable lithium ion battery cathodes. The aforementioned characteristics of RGO are generally "attributed" to the increases in performance of the composite electrodes, albeit without significant evidence beyond empirical cycling and/or capacity measurements. We have now conducted a systematic examination of the electrochemical response of an α-MnO_2-RGO composite while also investigating the role of the commonly observed nanowire morphology of α-MnO_2. The choice of α-MnO_2 follows from the challenges in reversibly cycling lithium ions over a large voltage window. Through the use of such a material, the objective is to amplify and observe the effects of the RGO to better understand the origin of the enhancements.

EXPERIMENTAL SECTION

Material Synthesis and Characterization. GO was synthesized using a modified Hummers method.[49] Briefly, 2 g of graphite powder was sonicated and stirred in an ice bath in 92 mL of conc. H_2SO_4 (Fisher 99%) with 2 g of $NaNO_3$ (Aldrich 99%) while 12 g of $KMnO_4$ (Aldrich 99%) was slowly added. Sonication continued for 30 min, after which the flask was removed and allowed to stir slowly overnight. Next, 100 mL of deionized (DI) H_2O was added slowly under nitrogen sparging followed by 1 h of stirring. Finally, 600 mL of 3% H_2O_2 (Fisher) was dispensed into the flask yielding a yellowish-brown GO suspension. The suspension was filtered and washed 3 times with conc. HCl, 10 times with 1 M HCl, and finally rinsed with copious amounts of DI H_2O. The GO remained suspended in DI water until aliquots were removed and dried for further use.

MnO_2 nanowires were synthesized using a modified version of literature reports.[50] $MnCl_2{\cdot}4H_2O$ (450 mg, 99.9% Alfa) was dissolved in isopropanol (Fisher) in a 3-neck flask under sonication and brought to reflux conditions (~80 °C). $KMnO_4$ (250 mg) was dissolved in 8 mL of DI H_2O and rapidly injected once the flask contents reached the required temperature. The temperature was then raised to boiling (~87 °C), and reaction progress was timed. Modifications included: (1) reflux at rapid boiling, (2) quenching at 5 min for short nanowires, and (3) quenching at 45 min for long nanowires. Upon completion of the reaction, precipitate was washed 3 times with 2:1 ethanol/water via centrifugation and was dried under vacuum at 60 °C for 8 h, after which it was ground with mortar and pestle for 2 min and stored in vials. RGO-MnO_2 composites were synthesized in an identical manner with the GO dried from suspension in a vacuum oven at 40 °C, weighed, and added to the isopropanol during $MnCl_2$ addition, with 30 minutes of sonication. Typically, 100 mg of GO was added.

Resulting materials were characterized using a Bruker D8 X-ray diffractometer, a Magellan 200 Field Emission Scanning Electron Microscope, and a Titan 80-300 Transmission Electron Microscope. X-ray diffraction (XRD) scans were performed from 2θ values 5°-80° with a 0.02 degree integration step size on powders pressed into a glass holder for preliminary characterization and on Al foil disk electrodes for postcycling characterizations with each specific sample preparation used consistently in comparisons (e.g., XRD on Al foil for both before and after cycling). Field emission scanning electron microscopy (SEM) images were obtained by drop casting a suspension of the material onto conductive fluorine-doped tin oxide and sputtering a 5 nm layer of gold using an EMITECH K550X sputter coater. Samples for transmission electron microscopy (TEM) were prepared by coating holey-carbon grids with a drop of dilute suspended material. Postcycled electrodes viewed via TEM were removed from the Al foil with *n*-methylpyrrolidinone (NMP), washed via centrifugation in NMP then ethanol, and finally suspended in ethanol for drop casting onto the TEM grid. Energy dispersive X-ray spectroscopy (EDXS) was obtained with the built-in X-ray detector in the Titan TEM. GO carbon−oxygen content was measured using a Costech Instruments ECS 4010 in oxygen analysis mode, and the mass of GO in the composites was calculated based on weight loss at 700 °C while accounting for the conversion of MnO_2 to Mn_3O_4.

dx.doi.org/10.1021/cs3001286 | ACS Catal. 2012, 2, 807−816

Scheme 1. Generalized Synthesis Procedure Followed for Generating RGO-Active Material Composites Used in Electrochemical Energy Storage Systems[a]

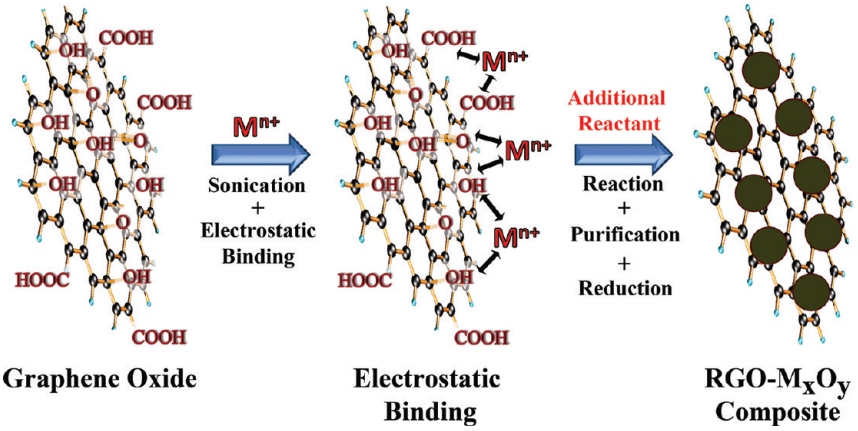

[a]Sonication facilitates exfoliation and complexation of metal cations, M^{n+}, via electrostatic binding. Finally, additional reaction and other purification steps follow to yield the RGO-M_xO_y (e.g. metal oxide) composite.

Electrochemical Measurements. A Gamry PCI4750 potentiostat was used for all electrochemical measurements. Electrochemical testing was performed using an internal test cell design (see Supporting Information, Figure S1) with lithium anode and 1 M $LiPF_6$ in 1/1/1 ethyl carbonate/dimethyl carbonate/diethylcarbonate w/w/w as electrolyte. Electrodes were prepared as 4″ × 4″ sheets on roughened and cleaned Al foil using a blading technique. The active powder was mixed thoroughly with 10% w/w carbon black while 10% w/w poly(vinylidene fluoride) was dissolved in *n*-methyl pyrrolidone (NMP). The NMP solution was added to the powder to create slurry, which was bladed onto the Al foil and dried at 120 °C under vacuum for 12 h. The electrode sheet was then stored under Ar with <0.1 ppm H_2O and O_2 until a 13 mm disk with mass between 15 and 20 mg was punched and used for testing. A copper current collector was used on the negative side with the Li disk, and polypropylene disk separated the cathode and Li. One drop of electrolyte was placed on the separator and 3 drops on the cathode, after which the electrodes were sandwiched, followed by a spacer and spring system and finally closure of the test cell.

Cyclic voltammetry (CV) was performed at a scan rate of 0.1 mV/s starting at open circuit. Initial scan direction was cathodic (toward 0 V vs Li/Li^+) to 2 V, then to 4.3 V, and back to open circuit after the desired number of scans. Charge−discharge cycling (CDC) was performed at various C rates calculated based on the weight of active MnO_2 in the electrode disk. Electrochemical impedance spectroscopy (EIS) was performed at 3 V vs Li/Li^+ following a CV scan at 10 mV/s to reduce residual GO prior to measurement. The battery was then driven to 3 V using chronoamperometry. Potentiostatic EIS was performed using a 10 mV rms perturbation in the frequency range of 100 kHz to 0.01 Hz. Gamry E-Chem Analyst software was used to fit the data to an equivalent circuit model. Chronocoulometry was performed from the same 3 V potential by stepping 5, 10, and 15 mV to generate discharge current (cathodic steps) for 30 s. Double step potential was 50 mV from 3 V and back to 3 V with 60 s duration for each step.

RESULTS

Synthesis and Characterization. The typical route for processing of RGO/GO-based composites involves common steps illustrated in Scheme 1 including: (a) mixing and interaction of GO and metal cations in solution via sonication, stirring, and so forth, (b) reaction of cationic species to generate active material, and (c) purification of the material and/or reduction of GO to RGO. The motivation for using such a synthesis route is to maximize loading of the active material on the GO surface through exfoliation of the larger aggregates of GO. Simultaneous exfoliation of GO sheets via sonication and electrostatic interaction between the GO surface-bound oxygen and the metal cations enables high loading of active material with intimate contact. Upon further reaction, ideally the growth of active material on GO sheets should prevent aggregation following removal of the composite from solution. This opens up channels between individual RGO sheets (or few-layer stacks) through which electroactive species such as Li^+ can diffuse. The channels naturally are on the scale of the active material dimensions, providing additional means for tuning the electrochemical response of these composites via material shape and size.

To synthesize the active material, we employed Mn compounds of two different oxidation states, Mn^{2+} and Mn^{7+} (i.e., $MnCl_2$ and $KMnO_4$) in isopropanol as previously reported,[50] to obtain tetragonal α-MnO_2 according to Reaction 1. The K^+ ions do not participate in the reaction but provide the cationic stability to the tunnel structures as the α-MnO_2 evolves via dissolution and recrystallization of the MnO_6 octahedral complexes. With the introduction of GO to the starting solution, we expect the Mn^{2+} cations to associate directly with the electronegative oxygens decorating the GO surface. Chen et al. proposed a growth mechanism whereby the GO oxygens participate in the MnO_6 octahedral complex.[50] Here, the reaction time was quenched at 5 and 45 min under reflux at boiling to yield short nanowires (SNW), RGO-SNW (rSNW) composite, long nanowires (LNW), and RGO-LNW (rLNW) composite, respectively.

$$2KMnO_4 + 3MnCl_2 + 2H_2O \rightarrow 5MnO_2 + 2KCl + 4HCl \quad (1)$$

XRD patterns were used to evaluate the impact of reaction quenching on crystallinity and to establish the phase(s) present in the material. The XRD patterns of SNW and LNW are

dx.doi.org/10.1021/cs3001286 | ACS Catal. 2012, 2, 807−816

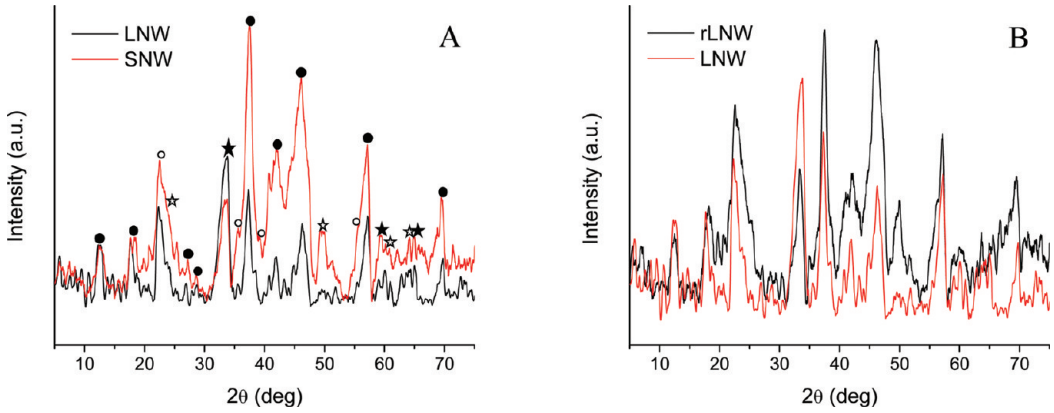

Figure 1. XRD scans of LNW and SNW. Panel A shows the SNW has slightly higher degree of crystallinity with closed circles representing α-MnO_2, open circles Ramsdellite MnO_2, closed stars Mn_3O_4, and open stars Mn_2O_3. Panel B shows the crystallinity for LNW is enhanced when GO is present while the impurity peak of Mn_3O_4 at 33° is reduced.

shown as an overlay in Figure 1A with the rLNW composite and LNW patterns overlay in Figure 1B. The patterns exhibit peaks consistent with α-MnO_2 (JCPDS No. 44-0141, a = 9.7845 Å, c = 2.8630 Å) as marked with closed circles in Figure 1A. Interestingly, the XRD pattern also indicates several peaks associated with Ramsdellite MnO_2 structure (marked with open circles), generating a mixed-morphology material similar to that reported previously.[27] Peaks attributed to partially oxidized Mn_2O_3 and Mn_3O_4 impurities arise and are denoted with open and filled stars in Figure 1A, respectively. XRD patterns of LNW with and without RGO (Figure 1B) showed higher intensities for most peaks in the rLNW composite. No evolution of a peak in the low-angle region representative of the interlayer spacing between GO (or RGO) sheets was observed. Either the dispersion of the nanowires between the single-to-few layer graphene stacks increased the interlayer spacing beyond that detectable within the scan angle or there exists insufficient long-range order in the composite to produce any coherent scattering by the RGO. This observation indicates that exfoliation of GO followed by subsequent material growth on the sheets prevents regular restacking of the GO-composite sheets, at least within the range of detection by low-angle scattering, and is in agreement with earlier findings.[51]

The starting amount of $KMnO_4$ was increased slightly above stoichiometric quantity in an attempt to eliminate the partially oxidized impurities, but they persisted, which is suggestive of a competing reaction. We suspect the impurities resulted from the oxidation of the C_3H_7OH with MnO_4^- ions, and the impurities were determined by redox titration with $KMnO_4$ to be between 4.3% and 6.3% w/w, depending on the actual ratio of Mn_2O_3 to Mn_3O_4 in the material (Supporting Information, Figure S2). The fraction of GO in the composite was also determined to be 38% w/w via thermal decomposition of GO at 700 °C while also accounting for the conversion of MnO_2 to Mn_3O_4. Water content was assumed negligible based on the postdrying process of the materials. From the starting ratio of materials and assuming complete conversion of Mn^{2+} to Mn^{4+}, the expected fraction of GO is calculated to be 34% by weight. Given the partially oxidized manganese oxide phases within the active material, the weight fraction should be higher than the theoretical value as observed. C−H−O analysis of the GO yields a fraction of 35% w/w for oxygen in the GO or a C:O atomic ratio of 2.4:1. This ratio would further decrease to C:O ~30:1 following electrochemical reduction[47] upon cycling of the composite electrode, after which the final RGO content is calculated to be 25% w/w.

The electrode macrostructure and the design of the nanowire composites were investigated using SEM. As depicted in Figure 2A the macrostructure of the RGO-supported nanowires

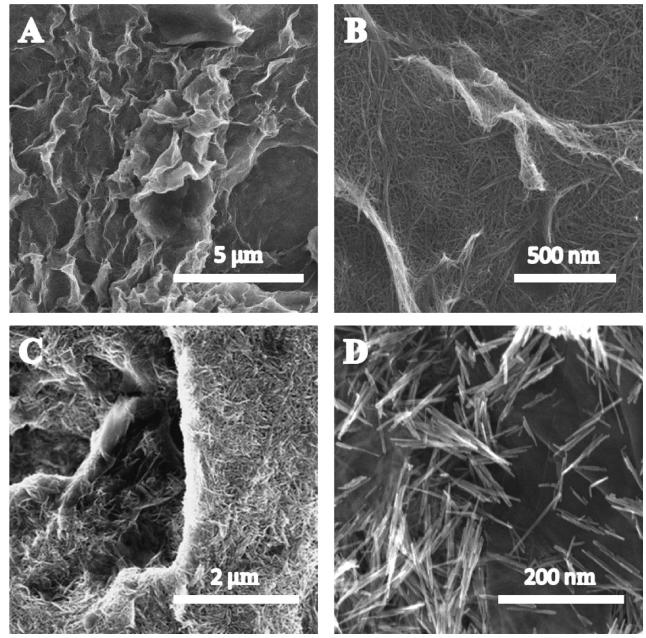

Figure 2. SEM micrographs of RGO-MnO_2 composites. (A) RGO 3-D macrostructure as depicted on an rLNW electrode surface. (B) rLNW composite with emphasis on the interconnected growth of the MnO_2 nanowires as well as the conformity of the nanowire to the RGO. (C) rSNW composite with the 3-D macrostructure evident. (D) rSNW composite at 250 kx depicts the SNW as having a length at least an order of magnitude less than LNW.

established a 3-D network and opened a large number of channels for electrolyte penetration into the depth of the electrode via the wrinkling of the RGO sheets. Figure 2B shows the rLNW composite. The ability of the nanowires to conform to the wrinkles and disorder of the RGO sheets indicates both good initial interactions between GO and Mn^{2+} starting materials as well as flexibility in the nanowire structure during extended synthesis time. Figures 2C and 2D represent the rSNW composite at 25 kx and 250 kx. The lengths of the

dx.doi.org/10.1021/cs3001286 | ACS Catal. 2012, 2, 807−816

nanowires in the rLNW composite were >5 μm while the rSNW nanowires were generally <500 nm. The rLNW composite exhibited interconnected "highways" of nanowires whereas the rSNW composite appeared more as needles than flexible wires. In all cases exceptional coverage of the RGO by the active material is observed.

TEM was performed on RGO and the MnO_2 nanowires to probe the morphology of the substrate and active material. Figures 3A and 3B show single-to-few layer RGO from which

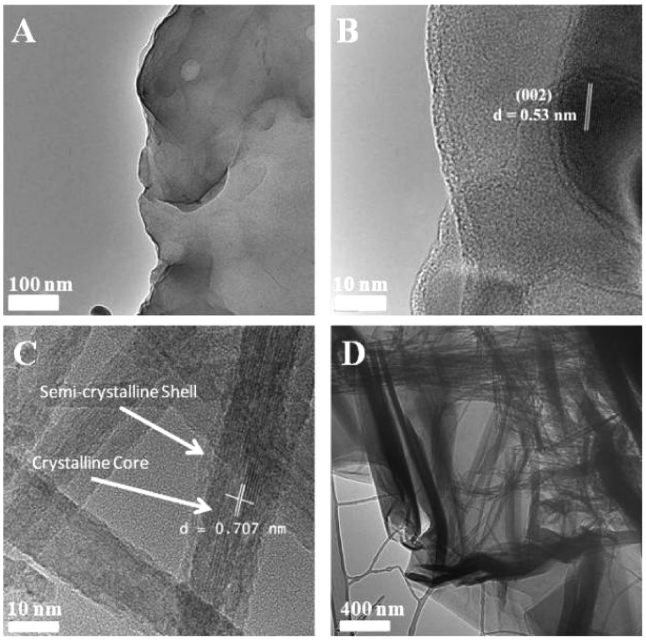

Figure 3. TEM micrographs of RGO composites and neat nanowires. (A) Few-layer-graphene stacks after undergoing reflux at boiling in isopropanol. (B) Intersection of three RGO sheets showing $d_{(002)}$ with an interlayer spacing of 5.3 Å. (C) Neat nanowires with the crystalline core measured at 7.07 Å, consistent with (110) of α-MnO_2 and semicrystalline shell, which is taken as partially oxidized manganese oxide impurities. (D) rLNW composite depicting curls and wrinkles associated with RGO edges.

the composites are constructed. The (002) d-spacing calculated at the intersection of the 3-layers in Figure 3B corresponds to an interlayer separation of 5.3 Å, slightly larger than that of pristine graphite (3.4 Å) but smaller than the 7−9 Å spacing typical for GO.[50,52] If we gauge the level of oxidation based on $d_{(002)}$, this would imply the sheets are considerably reduced during the synthesis with isopropanol likely acting as reducing agent. The LNW active material exhibits a d-spacing of 0.707 nm as determined from Figure 3C, which is consistent with the (110) plane of tetragonal α-MnO_2 and confirms the diffraction peak near 12° in the XRD patterns. The fact that the cores are crystalline and the edges are only semicrystalline supports the growth mechanism detailed previously.[50] Energy dispersive X-ray spectroscopy (EDXS) was used to estimate the potassium ion content within the α-MnO_2 (Supporting Information, Figure S3). The atomic percent of K^+ in the material was estimated to be 10.2% based on K-energy peaks with Mn at 32.8% and O at 57%, yielding a general formula of $K_{0.36}Mn_{1.15}O_2$ for LNW. The Mn:O ratio was 0.575, near the theoretical value of 0.5 with Mn-rich deviations stemming from the partially oxidized manganese oxides, which resulted in oxygen deficiency. Finally, the edge of the rLNW composite is shown across holey carbon grid in Figure 3D, depicting the curling and wrinkling of RGO at edges of sheets, which is thought to be responsible for the RGO 3-D macrostructure.

Electrochemical Cycling. Initial electrochemical cycling focused on CV to evaluate the intercalation potentials and possible side reactions within the voltage window chosen (2−4.3 V vs Li/Li^+). The CV scans were performed at 0.1 mV/s to provide sufficient time for equilibration of the capacitive MnO_2 and RGO components. Figure 4A shows the first scans for the LNW, SNW, and each composited with RGO. The scan progresses from open circuit to 2 V then to 4.3 V and finally returning to the original open circuit value (typically 3.4−3.5 V). Initial curves were spliced with data from the second scan to show completion of the full cycle. The prominent differences between the RGO-based electrodes and the neat electrodes are the extent of the electrochemical reactions and the onset potentials for these reactions. When anchored onto RGO the MnO_2 active material intercalates Li^+ to a greater extent as observed in the deeper cathodic response of the composites (rLNW and rSNW) and exhibits an additional oxidation peak near 3 V. Some of the initial cathodic current is expected to convert some portion of unreduced GO to RGO. Also, the rapid rise of anodic current between 4.2 and 4.3 V with the RGO composites is not reproduced with the neat materials, indicating that the RGO may act to catalytically oxidize the electrolyte solvent or serve to activate the MnO_2 active material to do so. The electrolyte oxidation potentials are slightly higher than these voltages on graphitic surfaces.[53]

The additional peak near 3 V during the anodic segment of the CV curve appears with the rSNW and rLNW electrodes, suggestive of impurity-phase oxidation with GO assisting in self-repair of the material to MnO_2. Partial contribution to this peak may be a result of additional discharging of stored electrons on the RGO surface,[49] or from expulsion of K^+. Additional CV cycles in Figure 4B show the flattening of the 3 V peak with near complete disappearance by the third cycle leading to the conclusion that the peak is representative of a transient reaction within the electrode. The irreversibility of this reaction further implies oxidation of residual $Mn^{2+/3+}$ to $Mn^{3+/4+}$ and/or the expulsion of a fraction of the stabilizing K^+ ions. The XRD patterns of the material after cycling the rLNW and LNW electrodes are shown in Figures 4C and 4D as an overlay with the initial pattern collected prior to cycling. The prominent peak at 49° corresponding to Mn_2O_3 decreases while Mn_3O_4 peaks at 33.5° and 60° increase for the rLNW, indicating some self-repair of the material when GO is present. Some slight decrease in these peaks was observed in the LNW sample but not to the extent of the rLNW, indicating GO may catalyze this reaction as well as supply oxygen as a reactant. Higher intensities were also recorded for a significant number of peaks corresponding with low-index planes of α-MnO_2 in rLNW suggesting that the growth of the Mn_3O_4 peak is only an intermediary between the Mn_2O_3 and full oxidation to MnO_2. Further study into this phenomenon is warranted to better understand how the GO facilitates the repair to MnO_2.

CDC was performed out to 10 cycles to evaluate the ability of the materials to cycle lithium reversibly at a rate of 0.4C, considered a good midpoint between low- and high-rate cycling. Figure 5A displays the CDC curves for the neat and composite electrodes, in addition to two important controls consisting of 30% carbon black and a physical mixture of RGO and LNW (r+LNW). The initial discharge was low for most electrodes albeit slightly higher for LNW and rLNW. This is

dx.doi.org/10.1021/cs3001286 | ACS Catal. 2012, 2, 807−816

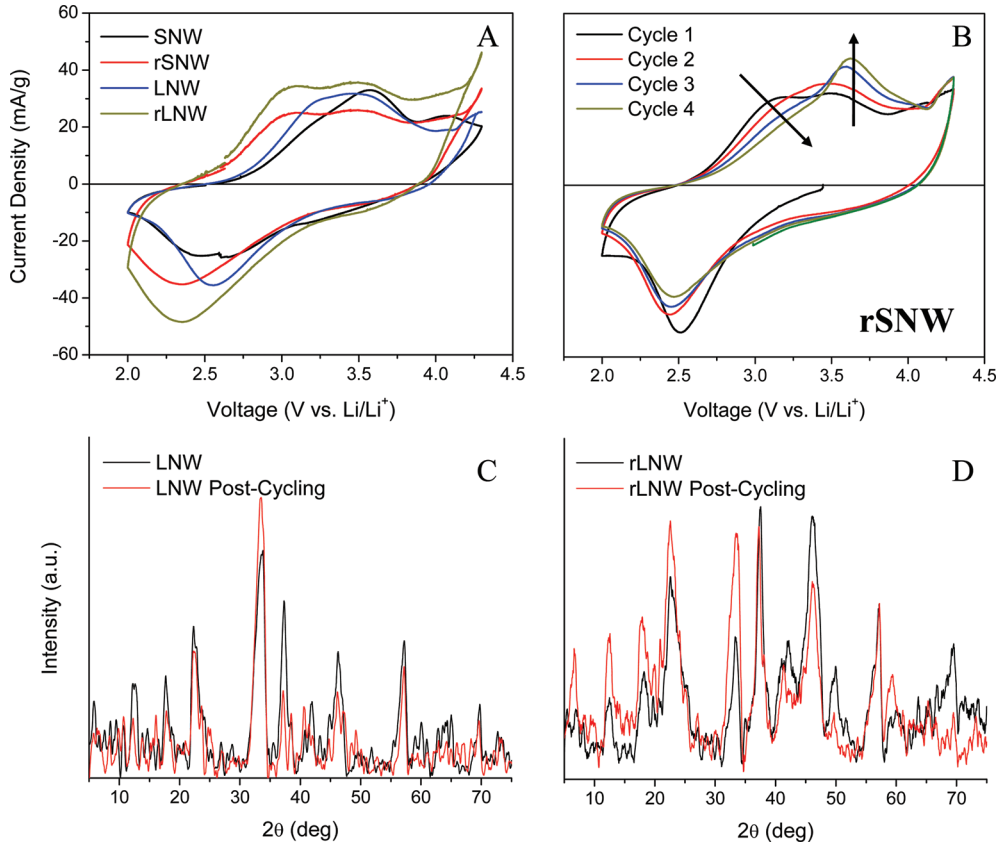

Figure 4. CV scans of SNW, LNW, and composites thereof accompanied by postcycling XRD analysis of impurities. (A) CV scan of neat and composite electrodes and (B) multiple scans of rSNW showing the gradual disappearance of the peak at 3 V. (C) and (D) XRD scans of LNW and rLNW before and after cycling show the self-repair of rLNW partially oxidized impurities.

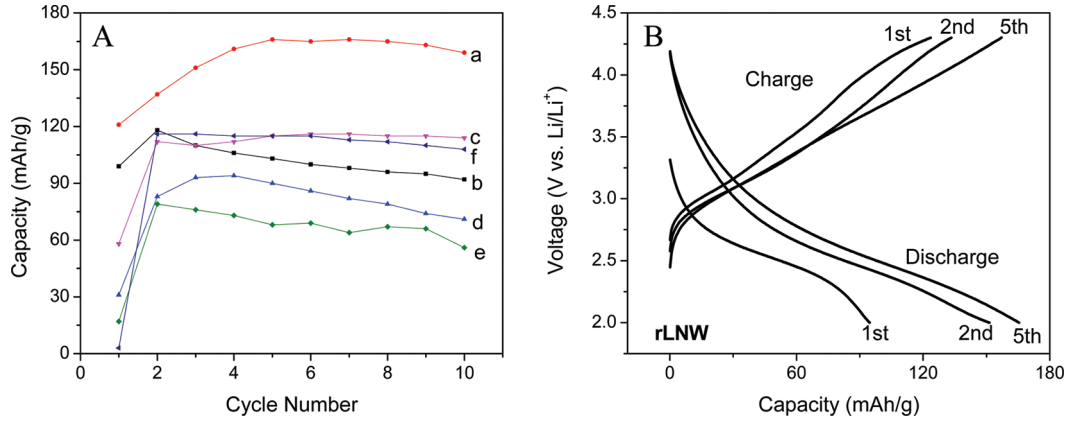

Figure 5. CDC summary. (A) Capacity vs cycling for (a) rLNW, (b) LNW, (c) rSNW, (d) SNW, (e) 30%C+LNW, (f) r+LNW. The rLNW achieves capacity well beyond the other electrodes at this cycling rate with rSNW appearing slightly more stable after 10 cycles. (B) 1st-5th charge–discharge cycles illustrating the large discrepancy between the initial discharge and the initial charge.

further illustrated in the voltage-capacity curves for the initial cycles of rLNW in Figure 5B. However, after the first charge cycle all materials recovered significantly with the rLNW composite continuing to increase in capacity with cycling up to about the fifth cycle. If we take the first discharge as a measure of residual K^+ within the tunnels, the LNW and rLNW retain the least amount of cation during synthesis with the implication that K^+ resides nearer surfaces than within the core of the structure since the core-to-surface ratio would be greater in the longer nanowires. Thus, the initial low discharge capacity may arise from residual K^+ in the MnO_2 lattice, while the initial high charge capacity represents the expulsion of the K^+ as well as any impurity oxidation as described in the CV experiments.

The rLNW composite exhibited the highest capacity and cycling stability at this rate. The rSNW composite was stable with increasing cycles but with less capacity than the rLNW. The controls (Figure 5A e,f) merely establish that the advantages realized via RGO are neither a result of additional carbon in the composite nor from the mere presence of RGO in the composite. Any enhancements observed in the RGO composites must therefore stem from both the 3-D macrostructure the RGO affords the electrode and the intimate

dx.doi.org/10.1021/cs3001286 | ACS Catal. 2012, 2, 807–816

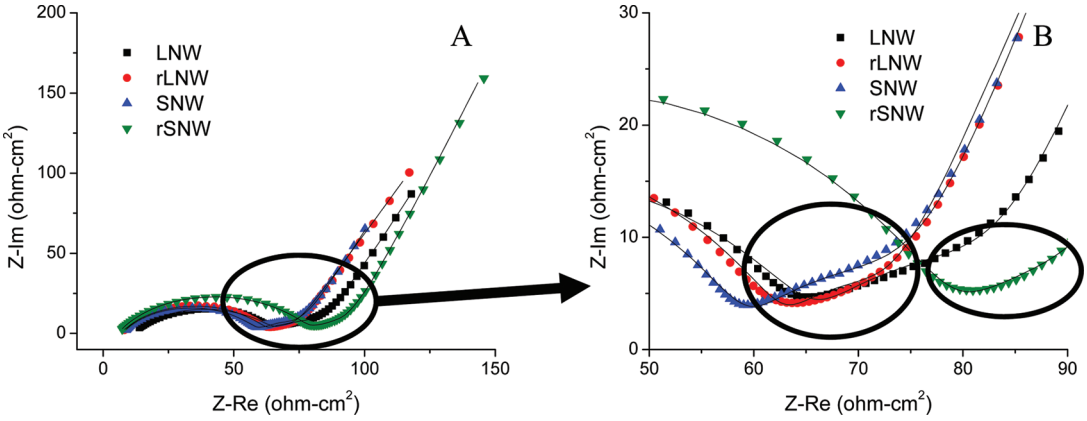

Figure 6. Impedance spectra for the neat and composite electrodes. Black circles represent the arc of interest, R_{ct}. (A) Nyquist plot of impedance spectra show the R-C offshoot between 50 and 75 Ω-cm^2 and the charge-transfer arc circled. (B) Zoom of the R_{ct} region of the spectra showing the slight arcs formed from the parallel R-C response.

contact between nanowires and RGO developed during synthesis. The mechanistic aspects of the enhancements afforded by the RGO are further elucidated in the additional electrochemical testing detailed in the next section.

Electrochemical Impedance and Chronocoulometry. EIS is a useful tool to gauge the impedances of an electrochemical cell. The primary interest in this study is in determination of the charge transfer resistance of the cathode. The charge transfer resistance, R_{ct}, is a parameter indicative of the ease of redox reactions at the electrode surface, although in the case of lithium ion intercalation, the redox reaction does not necessarily occur at the electrode−electrolyte interface. This would imply that the impedances for charge transfer resistance may also include resistances associated with Li^+ diffusion and electron migration through the MnO_2 lattice. Figure 6 shows the Nyquist plots of the MnO_2 and RGO-MnO_2 composites. (EIS spectra for 30% carbon and physical mix controls are provided in Supporting Information, Figure S4 along with the equivalent circuit used to fit impedance spectra). The charge transfer resistance follows the general trend observed in the CDC results with the lowest value reported for R_{ct} at 14.7 Ω-cm^2 for rLNW compared with 20.4 Ω-cm^2 for LNW. The rSNW composite exhibited R_{ct} = 20.9 Ω-cm^2 compared with 22.1 Ω-cm^2 for SNW. R_{ct} for the 30% carbon was 58.2 Ω-cm^2 along with 36.7 Ω-cm^2 for the RGO+LNW physical mixing. In general R_{ct} decreased when MnO_2 was anchored on the RGO substrate, although considerably more with the longer nanowires. The electrochemical response of the electrodes also dictated a series R-C element within the circuit as evidenced in the greater than 45° offshoot of the typical Warburg resistance. This effect was attributed to the capacitive effect of adsorbed species, which generated a pronounced R-C response in the spectra following the potentiostatic sinusoidal perturbation of the electrode.

R_{ct} generally follows the trends observed in the 10-cycle CDC testing shown above, although we expect higher surface area afforded in the SNW composite to produce better Li^+ storage behavior. The length of the nanowire must influence the total capacity realized during cycling in other ways. Other researchers have pointed out the stability of mixed morphology MnO_2 is achieved via segregation of Mn^{3+} ions into mixed-valence Mn^{3+}/Mn^{4+} zones surrounded by Mn^{4+} zones.[54] Assuming our material behaves in a similar manner, we expect the longer nanowires to accommodate the zoning effect much better than the shorter nanowires and to open up additional capacity since more zones can effectively inhabit a longer one-dimensional (1-D) structure. Even though the SNW would certainly have higher surface area as a result of higher terminal facets, the competing interest of Mn^{3+} stability leads to higher total capacity in both LNW/rLNW compared to SNW/rSNW. TEM micrographs of the post CDC rLNW are shown in Figure 7. When compared with the neat material (Figure 3C) it is readily apparent that zones of various polycrystalline phases are established during CDC. The (001) plane of α-MnO_2 was identified in Figure 7B with d = 0.29 nm.

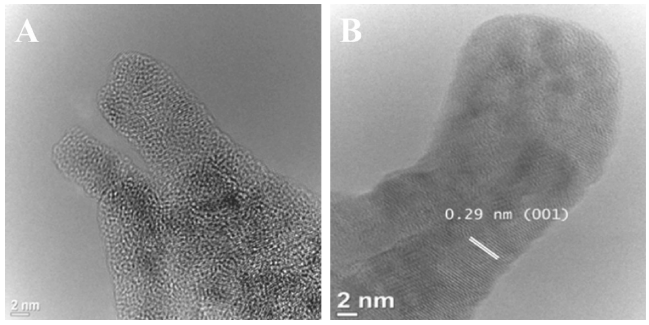

Figure 7. TEM micrographs of rLNW postcycling. (A) Tip of a single nanowire shows multitudes of oriented crystalline phases, attributed to segregation of Mn^{3+}/Mn^{4+} and Mn^{4+} zones. The tip of the nanowire also appears split as a result of the expansion-contraction effect upon lithium cycling. (B) Tip of another LNW within the composite further illustrating the polycrystalline phases with the identification of α-MnO_2 (001). The nanowires are curled and do not appear as rigid as those in Figure 3C, owing to the flexibility of the LNW morphology.

Chronocoulometry was employed to evaluate kinetic (k_f), diffusion (D_o), and charging (Q_{dl}) parameters as well as Li^+ adsorbate (Γ_o) for the electrodes. Kinetic parameters were calculated based on the electrochemical response to small potential steps over very short time scales (e.g., millisecond). Three step potentials (5, 10, and 15 mV from open circuit) were recorded, and the data for each step was fit to the linear form of the kinetic-regime dynamic response discussed by Bard and Faulkner,[55] eq 2. Satisfactory fits were obtained following the constraints of negative intercept and $Ht^{1/2} > 5$ within the range investigated.

dx.doi.org/10.1021/cs3001286 | ACS Catal. 2012, 2, 807−816

Table 1. Summary of Chronocoulometric Analysis for SNW, LNW, and RGO Composites Thereof[a]

	$k_f \times 10^7$ (cm/s/g)						
electrode	η = 5 mV	η = 10 mV	η = 15 mV	slope	$D_o \times 10^4$ (cm^2/s)	Q_{dl} (mC/g)	$\Gamma_o \times 10^7$ (mol/cm^2/g)
SNW	1.58	3.11	4.57	0.3	8.8	442.83	15.3
rSNW	4.42	8.61	12.2	0.8	10.5	628.3	9.44
LNW	1.57	3.01	4.33	0.3	7.5	428.8	16.7
rLNW	5.49	14.7	23.9	2	9.5	551.3	23.4
LNW+30%C	1.41	2.89	4.28	0.3	4.6	254.4	6.42
r+LNW	1.01	1.27	1.89	0.1	2.9	125.1	2.77

[a]Values are normalized to the mass of active MnO_2 within the electrode.

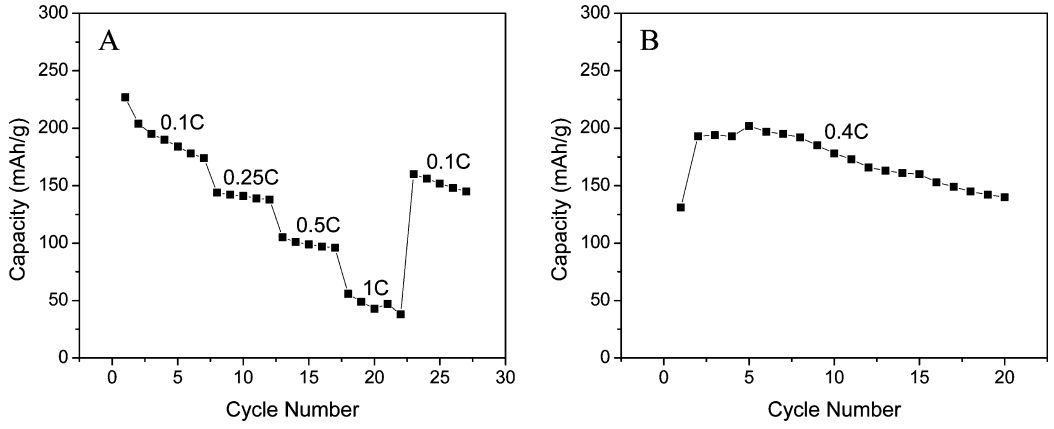

Figure 8. CDC summary for rLNW. (A) rLNW cycled at various rates with charge-initiated cycling. (B) rLNW cycled at 0.4C with discharge-initiated cycling between 1.9 and 4.2 V rather than the prior 2−4.3 V window.

$$Q(t) = nFAk_fC^*_o\left(\frac{2t^{1/2}}{H\pi^{1/2}} - \frac{1}{H^2}\right) \quad (2)$$

where n is the number of electrons in the reaction, F is Faraday's constant, A is the electrode area, k_f is the forward rate constant, C^*_o is the bulk concentration of the oxidized species in the electrolyte, $t^{1/2}$ is the experimental time raised to the power of 0.5, and $H = (k_f/D_o^{1/2}) + (k_b/D_R^{1/2})$ with k_b as the backward rate constant and D_R the diffusion of the reduced species. In the form of the equation above, H is evaluated using the y-intercept of Q vs $t^{1/2}$ via the relation $H = \pi^{1/2}/t_i^{1/2}$.

The kinetic rate constant, k_f, calculated for each step potential was also plotted as a function of overpotential while forcing the function to zero. Linear fits of these plots resulted in R^2 values greater than 0.97 with the exception of r+LNW (physically mixed RGO and MnO_2), indicating the current response to applied overpotential is linear, as expected if the electrode step potentials are within the current regime given by linearization of Butler−Volmer, $j = j_o f\eta$, where j is current density, j_o is exchange current density, $f = F/RT$, and η is the applied overpotential. Other parameters were evaluated using a double step regime. Double step potentials were 50 mV from open circuit and back to open circuit, and the resulting parameters including D_o, Q_{dl}, and Γ_o were calculated from the Cotrell equation coupled with Anson plots of the chronocoulometric responses. Table 1 summarizes these results for the neat and composite electrodes as well as the controls.

The major findings from the chronocoulometry results are as follows: (1) RGO composites exhibited higher forward rate constants, k_f, with rLNW achieving the highest rate and largest slope (implying greater increases in k_f with increasing overpotential), (2) RGO composites significantly enhanced diffusion of the Li^+ to the active intercalation sites, (3) RGO increased Q_{dl} as expected given that RGO is known to store electrons on its surface,[49] and (4) both excess carbon and physically mixed RGO/LNW generated poor electrode response. Findings (1) and (2) validate the CDC data for the neat and composite electrodes, as enhanced forward rates and higher diffusion rates would naturally lead to higher capacity within a given voltage window for either rSNW or rLNW when compared to SNW or LNW. The higher D_o values measured in the RGO composites facilitate extended cycling stability by reducing the lifetime of polarized Mn^{3+} ions without the stabilizing effect of Li^+. Further, the higher Q_{dl} values associated with RGO provide an opportunity to polarize the RGO rather than the active material via buildup of electrons on the RGO surface. It is likely that a length-related RGO-nanowire synergistic effect is responsible for the amount of adsorbed Li^+ on the electrode surface.

The buildup of electrons on RGO with subsequent discharge to intercalation sites upon arrival of Li^+ would further minimize the Jahn−Teller electronic instabilities of Mn^{3+} and enhance electrode life. In this role the RGO serves as kinetic mediator of the intercalation reaction by allowing buildup of electrons on its surface rather than the surface of MnO_2 while *concurrently* reducing the arrival time of diffusing Li^+. We also observe that merely adding more carbon actually contributed to a decline in the electrode response as did physically mixing the RGO with nanowires. Altogether these results confirm the 2-D RGO structure facilitating good nanowire dispersion, strong RGO interactions developed during exfoliation/synthesis, and the higher diffusion rates afforded via the 3-D RGO macrostructure are responsible for net enhancements realized in RGO-MnO_2 composites.

Extended CDC of rLNW Electrode. While our objective to probe the influences of RGO on the electrochemical

dx.doi.org/10.1021/cs3001286 | ACS Catal. 2012, 2, 807−816

properties of the active material was met, further cycling was performed on the rLNW material to evaluate the performance at various rates and extended cycling. The rLNW was cycled in the progression of 0.1C, 0.25C, 0.5C, 1C, and returning to 0.1C, and at 0.4C for full 20 cycles. We opted first to test the electrode stability by initiating with a charge cycle rather than a discharge cycle. The cycling results shown in Figure 8A point to less stability than was observed in the 10 cycles in Figure 6A, even at the lower cycle rate, which is attributed to significant removal of K^+ stabilizing ions within the tunnels of the MnO_2 structure during the initial charge at low rate. Capacity retention at 0.1C relative to the second discharge was found to be 72% for the charge-initiated cycling. The initial charge capacity was 101 mAh/g, or about 35% of the theoretical capacity. This value is similar to the calculated atomic percent of K^+ from EDXS measurements, pointing to K^+ expulsion during this initial charge along with oxidation of $Mn^{2+/3+}$ impurities as previously shown. Figure 8B depicts a fresh rLNW electrode cycled at 0.4C for 20 cycles while changing the voltage window to 1.9−4.2 V vs Li/Li^+ to avoid the high oxidation currents in the CV scan between 4.2 and 4.3 V.

The loss in capacity with increasing cycles in Figure 8A is attributed mostly to the removal of the stabilizing cations (K^+) with the charge-initiated cycling. These cations are necessary for the stability obtained in the previous CDC testing. By intercalating Li^+ with the K^+ ions remaining, the lattice maintains the larger unit cell spacing and accommodates the Li^+ without significant issue. Cycling the material at low rate (0.1C) potentially further exacerbates the irreversibility problem by also removing and inserting high Li^+ content, leading to mechanical destabilization of the active material through significant expansion-contraction. By changing the cycling voltage window we were able to achieve significantly higher capacity at 0.4C than the previous 10 cycles in Figure 6A with a peak capacity of 202 mAh/g at cycle 5. However, after ∼9 cycles, irreversibility began to set in, albeit at a low rate with the rLNW still able to deliver close to 150 mAh/g at this rate after 20 cycles. Further exploration of the voltage windows is warranted to maximize the utility of this composite material, as 1.9 V vs Li/Li^+ likely amplified reduction of Mn^{3+} to Mn^{2+} with subsequent dissolution in the electrolyte and loss of active material. The fact that we see increased reversible behavior at higher rates would suggest that some polarization of the electrode supports reversible cycling by limiting the amount of Li^+ inserted and removed within the voltage window.

CONCLUSIONS

RGO serves as a conductive support for α-MnO_2 nanowires and increases the performance of the storage battery in terms of cycling and capacity through a combination of kinetic, mass transfer, and capacitive enhancements. Owing to the ability of RGO to store electrons in its $\pi-\pi$ network, we conclude that RGO acts as a kinetic mediator between electrons and Li^+ ions in the electrolyte by discharging stored electrons more rapidly to intercalation sites while facilitating rapid diffusion of Li^+ through the electrode matrix. Additionally, the RGO enables additional expulsion of ions from the MnO_2 lattice as observed in CV scans and enhances crystallinity and self-repair of impurity phases within the MnO_2. Extended cycling of the best-performing composite, consisting of RGO and long nanowires, show the challenges associated with the irreversibility of this material still persist. Further investigation of a voltage window conducive to fully reversible cycling can potentially alleviate these long-term issues with α-MnO_2.

ASSOCIATED CONTENT

Supporting Information

Battery test cell images and design, impurity titration data, EDXS spectra, EIS spectra for controls, and EIS equivalent circuit model. This material is available free of charge via the Internet at http://pubs.acs.org.

AUTHOR INFORMATION

Corresponding Author

*E-mail: pkamat@nd.edu.

Funding

The authors thank TARDEC for support of lithium ion battery research at the University of Notre Dame. This is NDRL 4914 from the Notre Dame Radiation Laboratory, which is supported by the Division of Chemical Sciences, Geosciences and Biosciences, Office of Basic Energy Sciences of the U.S. Department of Energy.

Notes

The authors declare no competing financial interest.

ACKNOWLEDGMENTS

We thank Jim Strope of the Notre Dame Radiation Laboratory for constructing the battery test cell as well as Paul McGinn of the Department of Chemical & Biomolecular Engineering Department at University of Notre Dame for fruitful discussions surrounding the research presented herein.

REFERENCES

(1) Ryu, W.-H.; Eom, J.-Y.; Yin, R.-Z.; Han, D.-W.; Kim, W.-K.; Kwon, H.-S. *J. Mater. Chem.* **2011**, *21*, 15337−15342.
(2) Zhao, X.; Hayner, C. M.; Kung, H. H. *J. Mater. Chem.* **2011**, *21*, 17297−17303.
(3) Qing, C.; Bai, Y.; Yang, J.; Zhang, W. *Electrochem. Acta* **2011**, *56*, 6612−6618.
(4) Qu, Q.; Fu, L.; Zhan, X.; Samuelis, D.; Maier, J.; Li, L.; Tian, S.; Li, Z.; Wu, Y. *Energy Environ. Sci.* **2011**, *4*, 3985−3990.
(5) Dimesso, L.; Spanheimer, C.; Jacke, S.; Jaegermann, W. *J. Power Sources* **2011**, *196*, 6729−6734.
(6) Ma, J.; Li, B.; Du, H.; Xu, C.; Kang, F. *Electrochem. Acta* **2011**, *56*, 7385−7391.
(7) Chen, W.-M.; Huang, Y.-H.; Yuan, L.-X. *J. Electroanal. Chem.* **2011**, *660*, 108−113.
(8) Saji, V. S.; Kim, Y.-S.; Kim, T.-H.; Cho, J.; Song, H.-K. *Phys. Chem. Chem. Phys.* **2011**, *13*, 19226−19237.
(9) Niu, B.; Qi, E.-l.; Wang, J.-q. *J. Inorg. Organomet. Polym. Mater.* **2011**, *21*, 906−912.
(10) Zhou, F.; Zhao, X.; Liu, Y.; Li, L.; Yuan, C. *J. Phys. Chem. Solids* **2008**, *69*, 2061−2065.
(11) Fan, G.; Zeng, Y.; Chen, R.; Lue, G. *J. Alloys Compd.* **2008**, *461*, 267−272.
(12) Liu, Q.; Li, Y.; Hu, Z.; Mao, D.; Chang, C.; Huang, F. *Electrochim. Acta* **2008**, *53*, 7298−7302.
(13) Li, X.; Liu, D.; Zhang, D.; Chen, X.; Tian, X. *J. Phys. Chem. Solids* **2009**, *70*, 936−940.
(14) Zhao, C.; Kang, W.; Zhao, S.; Shen, Q. *Micro Nano Lett.* **2010**, *6*, 820−822.
(15) Girishkumar, G.; McCloskey, B.; Luntz, A. C.; Swanson, S.; Wilcke, W. *J. Phys. Chem. Lett.* **2010**, *1*, 2193−2203.
(16) Devaraj, S.; Munichandraiah, N. *J. Phys. Chem. C* **2008**, *112*, 4406−4417.
(17) Yu, D. S.; Dai, L. M. *J. Phys. Chem. Lett.* **2009**, *1*, 467−470.

(18) Yang, H.; Jiang, J.; Zhou, W.; Lai, L.; Xi, L.; Lam, Y. M.; Shen, Z.; Khezri, B.; Yu, T. *Nanoscale Res. Lett.* **2011**, *6*.
(19) Yu, G.; Hu, L.; Liu, N.; Wang, H.; Vosgueritchian, M.; Yang, Y.; Cui, Y.; Bao, Z. *Nano Lett.* **2011**, *11*, 4438−4442.
(20) Wang, J.-G.; Yang, Y.; Huang, Z.-H.; Kang, F. *Electrochim. Acta* **2011**, *56*, 9240−9247.
(21) Babakhani, B.; Ivey, D. G. *J. Power Sources* **2011**, *196*, 10762−10774.
(22) Shen, Y. F.; Zerger, R. P.; Deguzman, R. N.; Suib, S. L.; McCurdy, L.; Potter, D. I.; Oyoung, C. L. *Science* **1993**, *260*, 511−515.
(23) Boppana, V. B. R.; Jiao, F. *Chem. Commun.* **2011**, *47*, 8973−8975.
(24) Qiu, G.; Huang, H.; Dharmarathna, S.; Benbow, E.; Stafford, L.; Suib, S. L. *Chem. Mater.* **2011**, *23*, 3892−3901.
(25) Kalubarme, R. S.; Cho, M.-S.; Yun, K.-S.; Kim, T.-S.; Park, C.-J. *Nanotechnology* **2011**, 22.
(26) Paez, C. A.; Liquet, D. Y.; Calberg, C.; Lambert, S. D.; Willems, I.; Germeau, A.; Pirard, J.-P.; Heinrichs, B. *Catal. Commun.* **2011**, *15*, 132−136.
(27) Johnson, C. S.; Mansuetto, M. F.; Thackeray, M. M.; Shao-Horn, Y.; Hackney, S. A. *J. Electrochem. Soc.* **1997**, *144*, 2279−2283.
(28) Liu, Y.; Fujiwara, T.; Yukawa, H.; Morinaga, M. *Solid State Ionics* **1999**, *126*, 209−218.
(29) Aydinol, M. K.; Ceder, G. *J. Electrochem. Soc.* **1997**, *144*, 3832−3835.
(30) Sherman, D. M. *Am. Mineral.* **1984**, *69*, 788−799.
(31) Hashem, A. M.; Abdel-Latif, A. M.; Abuzeid, H. M.; Abbas, H. M.; Ehrenberg, H.; Farag, R. S.; Mauger, A.; Julien, C. M. *J. Alloys Compd.* **2011**, *509*, 9669−9674.
(32) Hashem, A. M.; Abuzeid, H. M.; Narayanan, N.; Ehrenberg, H.; Julien, C. M. *Mater. Chem. Phys.* **2011**, *130*, 33−38.
(33) Johnson, C. S. *J. Power Sources* **2007**, *165*, 559−565.
(34) Johnson, C. S.; Dees, D. W.; Mansuetto, M. F.; Thackeray, M. M.; Vissers, D. R.; Argyriou, D.; Loong, C. K.; Christensen, L. *J. Power Sources* **1998**, *75*, 183−184.
(35) Wang, Y.; Liu, H.; Bao, M.; Li, B.; Su, H.; Wen, Y.; Wang, F. *J. Alloys Compd.* **2011**, *509*, 8306−8312.
(36) Ding, Y.; Jiang, Y.; Xu, F.; Yin, J.; Ren, H.; Zhuo, Q.; Long, Z.; Zhang, P. *Electrochem. Commun.* **2010**, *12*, 10−13.
(37) He, Y. S.; Bai, D. W.; Yang, X. W.; Chen, J.; Liao, X. Z.; Ma, Z. F. *Electrochem. Commun.* **2010**, *12*, 570−573.
(38) Wu, Z. S.; Ren, W. C.; Wen, L.; Gao, L. B.; Zhao, J. P.; Chen, Z. P.; Zhou, G. M.; Li, F.; Cheng, H. M. *ACS Nano* **2010**, *4*, 3187−3194.
(39) Zhang, L. S.; Jiang, L. Y.; Yan, H. J.; Wang, W. D.; Wang, W.; Song, W. G.; Guo, Y. G.; Wan, L. J. *J. Mater. Chem.* **2010**, *20*, 5462−5467.
(40) Du, Z. F.; Yin, X. M.; Zhang, M.; Hao, Q. Y.; Wang, Y. G.; Wang, T. H. *Mater. Lett.* **2010**, *64*, 2076−2079.
(41) Zhou, G. M.; Wang, D. W.; Li, F.; Zhang, L. L.; Li, N.; Wu, Z. S.; Wen, L.; Lu, G. Q.; Cheng, H. M. *Chem. Mater.* **2010**, *22*, 5306−5313.
(42) Wang, H. L.; Cui, L. F.; Yang, Y. A.; Casalongue, H. S.; Robinson, J. T.; Liang, Y. Y.; Cui, Y.; Dai, H. J. *J. Am. Chem. Soc.* **2010**, *132*, 13978−13980.
(43) Yu, A.; Park, H. W.; Davies, A.; Higgins, D. C.; Chen, Z.; Xiao, X. *J. Phys. Chem. Lett.* **2011**, *2*, 1855−1860.
(44) Kim, H.; Kim, S.-W.; Hong, J.; Park, Y.-U.; Kang, K. *J. Mater. Res.* **2011**, *26*, 2665−2671.
(45) Kamat, P. V. *J. Phys. Chem. Lett.* **2011**, *2*, 242−251.
(46) Hummers, W. S.; Offeman, R. E. *J. Am. Chem. Soc.* **1958**, *80*, 1339−1339.
(47) Dreyer, D. R.; Park, S.; Bielawski, C. W.; Ruoff, R. S. *Chem. Soc. Rev.* **2010**, *39*, 228−240.
(48) Radich, J. G.; McGinn, P.; Kamat, P. V. *Interface* **2011**, *63*, 63−66.
(49) Lightcap, I. V.; Kosel, T. H.; Kamat, P. V. *Nano Lett.* **2010**, *10*, 577−583.
(50) Chen, S.; Zhu, J.; Wu, X.; Han, Q.; Wang, X. *ACS Nano* **2010**, *4*, 2822−2830.
(51) Xu, C.; Wang, X.; Zhu, J. *J. Phys. Chem. C* **2008**, *112*, 19841−19845.
(52) Shao, Y.; Wang, J.; Engelhard, M.; Wang, C.; Lin, Y. *J. Mater. Chem.* **2010**, *20*, 743−748.
(53) Arakawa, M.; Yamaki, J. *J. Power Sources* **1995**, *54*, 250−254.
(54) Umek, P.; Gloter, A.; Pregelj, M.; Dominko, R.; Jagodic, M.; Jaglicic, Z.; Zimina, A.; Brzhezinskaya, M.; Potocnik, A.; Filipic, C.; Levstik, A.; Arcon, D. *J. Phys. Chem. C* **2009**, *113*, 14798−14803.
(55) Bard, A. J.; Faulkner, L. R. *Electrochemical Methods - Fundamentals and Applications*, 2nd ed.; John Wiley & Sons, Inc.: New York, 2001.